PAPER

Simulation of magneto-induced rearrangeable microstructures of magnetorheological plastomers†

Taixiang Liu,[a] Xinglong Gong,*[a] Yangguang Xu,[a] Shouhu Xuan[a] and Wanquan Jiang[b]

Magneto-induced microscopic particulate structures of magnetorheological plastomers (MRP) are investigated using particle-level dynamics simulation, as this is a basis for studying the macroscopic physical or mechanical properties of MRP. In the simulation, a modified magnetic dipolar interaction force model is proposed to describe the magnetic interaction of two close magnetized iron particles. Other microscopic analytical models of particle–particle and particle–matrix interactions are also constructed. The simulation results show that chain-like and column-like particulate structures are formed when MRP is placed into a steady uniform magnetic field. When MRP is subjected to a stepwise in-plane rotating magnetic field, the microstructure rearranges to form a layered structure parallel to the rotation plane. Moreover, some other patterns or complex magneto-induced rearrangeable microstructures can be achieved by spatially changing the external magnetic field. With the evolution of the microscopic particulate structure in every changing step of the external magnetic field, the microstructure dependent magnetic potential energy and stress state vary sharply at the beginning and then approach respective stable values gradually.

1 Introduction

Magnetorheological plastomers (MRP), as reported and discussed in our group's previous work,[1–3] are a new type of smart magnetorheological material. In general, MRP are prepared by dispersing micron-sized soft magnetic particles into a plastic matrix. In the absence of an external magnetic field, the particles are fixed in specific positions due to the constraint of the matrix. But the particles can arrange into some ordered microstructures in an external magnetic field, or rearrange into some new microstructures with the changing of the external magnetic field. These inherent properties give the MRP novel performances in rheology and much potential in practical applications.

Other magnetorheological materials, generally having micron-sized soft magnetic particles as the dispersing phase and mainly differing in their matrix, include magnetorheological fluids,[4–8] magnetorheological elastomers,[9–12] magnetorheological gels,[13–17] magnetorheological foams[18–20] and some other species. The rheological properties of these magnetorheological materials can be altered by an external magnetic field. With these magnetic controllable properties, magnetorheological materials have attracted much attention of researchers and have many applications. Typical applications of magnetorheological fluids include automotive clutches, brakes for exercise equipment, polishing fluids, actuator systems, seismic vibration dampers, control valves, artificial joints, and shock absorbers.[6,21] Magnetorheological elastomers have been used in dampers, adaptive seismic isolators, adaptive tuned vibration absorbers, tuneable stiffness mounts and piezoelectric power actuators.[10,12,22] When the magnetic dispersing phases are nano-sized and the matrixes are fluid-like, these mixtures are usually named as magnetic suspensions[23–26] or magnetic fluids,[27,28] as the nano-sized dispersing phase generally has a permanent single magnetic domain. Magnetic fluids have already been used in rotary seals, magnetic clutches and tunable dampers.[28] Besides the above and more broadly speaking, there are also many morphing soft magnetic composites.[29] Generally, an ideal magnetorheological material should possess long-time stability and a large magnetorheological effect. Fortunately, MRP can overcome the headache of the particle sedimentation problem of magnetorheological fluids[30] and show a much higher magnetorheological effect than magnetorheological elastomers.[1]

It is widely recognised that the physical properties or the mechanical performance of magnetorheological materials are directly related to the interior particle-formed microstructures, and it is known how these microstructures change with external

[a]CAS Key Laboratory of Mechanical Behavior and Design of Materials, Department of Modern Mechanics, University of Science and Technology of China, Hefei, Anhui, 230027, China. E-mail: gongxl@ustc.edu.cn; Fax: +86 551 63600419; Tel: +86 551 63600419

[b]Department of Chemistry, University of Science and Technology of China, Hefei, Anhui, 230027, China

† Electronic supplementary information (ESI) available. See DOI: 10.1039/c3sm52130c

magnetic fields. For example, Peng *et al.*[8] investigated the microstructure-based behaviour of magnetorheological fluids. Chen *et al.*[31] studied the microstructures and viscoelastic properties of anisotropic magnetorheological elastomers. The particle rearrangement during cyclic stress hardening of magnetorheological gels was directly observed and studied by An *et al.*[13] The rheological properties of MRP have been experimentally studied in our group's previous work.[1–3] However, the microstructure-based physical mechanism of these properties has not been investigated deeply. Especially, the fact that the soft magnetic particles can rearrange into some new microstructures with the changing of the external magnetic field should be paid more attention to, as this inherent characteristic makes MRP more magneto-controllable. However, to date, it has been very difficult or even impossible to directly observe the rearranging process of the interior soft magnetic particles of MRP in an experiment. To our knowledge, the particle-level dynamics simulation method has been widely used to investigate the microstructures and their evolution for many particle-dispersion materials, especially for magnetorheological fluids. It is worth trying to introduce the particle-level dynamics simulation method to investigate the microstructure of MRP and its evolution.

In this work, we try to construct a microscopic analytic model of MRP and give emphasis to the magneto-induced rearrangeable microstructure of MRP. In the next section, basic experimental tests of soft magnetic particles and the preparation process of MRP are presented. Meanwhile, the magnetization properties and size distribution of soft magnetic particles are characterized. In Section 3, the main models of particle–particle and particle–matrix interactions are discussed and presented for further kinematic simulation. The simulation results for the magneto-induced rearrangeable microstructure are presented in Section 4. In addition, the microstructure dependent magnetic potential energy and stress state are also discussed. Finally, some remarkable conclusions are summarized in Section 5.

2 Experimental

In this section, the magnetization and size distribution properties of soft magnetic particles are presented and characterized firstly. Then, a MRP sample was prepared and the microstructural SEM image of the MRP is shown. Moreover, the relationship between the shear stress and the shear rate of the MRP sample was tested and presented at the end of this section.

2.1 Physical properties of the soft magnetic particle

In the experiment, carbonyl iron powder (type CN, produced by BASF aktiengesellschaft, Germany) was used as the soft magnetic dispersing particle. The content of iron in this powder was no less than 99.5 wt%. Its true density was 7.20 g cm^{-3}, tested using the double pycnometer method. The particle is an iron core coated with a very thin oxidation layer. We term this carbonyl iron powder as "BASF-CIP-CN" in this paper. As Fig. 1 shows, the magnetization properties (tested by SQUID-VSM,
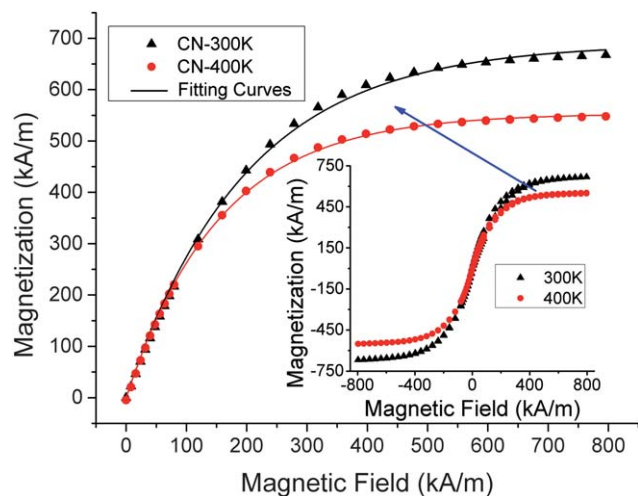

Fig. 1 Magnetization of BASF-CIP-CN *versus* external magnetic strength. The inset shows the whole magnetization curve with a negligible hysteresis loop.

Quantum Design Inc., USA) of BASF-CIP-CN can be described using the following equation:

$$M = M_s\left(1 - e^{-\chi H_{ext}}\right) \qquad (1)$$

where M and M_s are the magnetization and saturation magnetization, respectively. χ is the adaptive magnetization coefficient and H_{ext} is the strength of the external magnetic field. $M_s = 6.90 \times 10^5$ A m^{-1}, $\chi = 5.06 \times 10^{-6}$ m A^{-1} at a temperature of 300 K and $M_s = 5.54 \times 10^5$ A m^{-1}, $\chi = 6.42 \times 10^{-6}$ m A^{-1} at a temperature of 400 K.

The size distribution of BASF-CIP-CN (tested by BT-2001, Dandong Bettersize instruments Ltd, China) is shown in Fig. 2 and can be described by the lognormal distribution function as:

$$P(d) = \frac{1}{d\sigma\sqrt{2\pi}}\exp\left[-\frac{(\ln(d) - \mu)^2}{2\sigma^2}\right]. \qquad (2)$$

Here, $P(d)$ is the probability density function of the particle and d denotes the diameter of the particle. $\mu = 1.96$
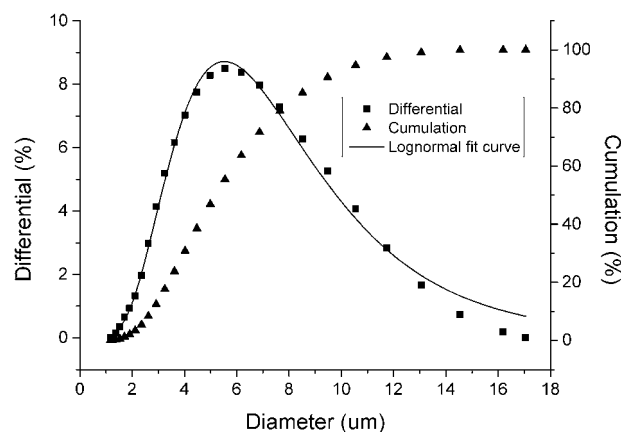

Fig. 2 Size distribution of BASF-CIP-CN. The size range is 1.31–17.05 μm with $d_{10} = 2.89$, $d_{50} = 5.46$ and $d_{90} = 9.88$ μm.

and $\sigma = 0.50$ are the expectation and variance of $\ln(d)$, respectively.

2.2 Synthesis of the matrix and preparation of the MRP sample

The preparation method of the MRP sample is the same as reported in our group's previous work.[2] The plastic matrix was synthesized from toluene diisocyanate (TDI, 2,4- $\approx$ 80%, 2,6- $\approx$ 20%, Tokyo Chemical Industry Co., Ltd, Japan) and polypropylene glycol (PPG-1000, Sigma-Aldrich (Shanghai) Trading Co., Ltd, China) with a weight ratio of 3 : 1. The raw materials were mixed in a three-necked round-bottom flask at 75 °C for two hours. Meanwhile, the reactants were stirred at all times with a stirrer through the middle neck of the flask. Then, the temperature was lowered to 65 °C, and 1,4-buta-nediol (BDO, Sinopharm Chemical Reagent Co., Ltd, China) was added as the chain extender. One hour later, a small quantity of stannous octoate and a moderate amount of acetone (both provided by Sinopharm Chemical Reagent Co., Ltd, China) were added dropwise into the flask to accelerate the cross linking reaction and to avoid gelating. Twenty minutes later, the synthesis process was finished.

Once the synthesis process of the matrix was finished, soft magnetic powder was added into the matrix immediately, which was adequately blended before the matrix cooled down. In our experiment, we added BASF-CIP-CN with a weight fraction of 70.0% to the whole mixture. We termed these polyurethane-based MRP as "MRP-70", both in the experimental and the subsequent simulation. The volume fraction of BASF-CIP-CN in MRP-70 was 24.2% (the density of pure polyurethane is 0.9858 g cm^{-3}). SEM images of MRP-70 are shown in Fig. 3. It can be seen that chain-like structures formed along the direction of the external magnetic field, while the particles dispersed uniformly when the MRP were in no external magnetic field.

The rheological properties of MRP-70 at room temperature (25 °C) are shown in Fig. 4. The shear stress–rate relationship can be described by the conventional Bingham model:

$$\tau = \tau_0 + \eta \cdot \dot{\gamma}, \tag{3}$$

where τ is the shear stress, τ_0 is the shear yield stress, η is the dynamic viscosity and $\dot{\gamma}$ is the shear rate. Here, from the view of the shear rate in the range of 0.0–5.0 s^{-1}, $\tau_0 = 4.16$ kPa and $\eta =$
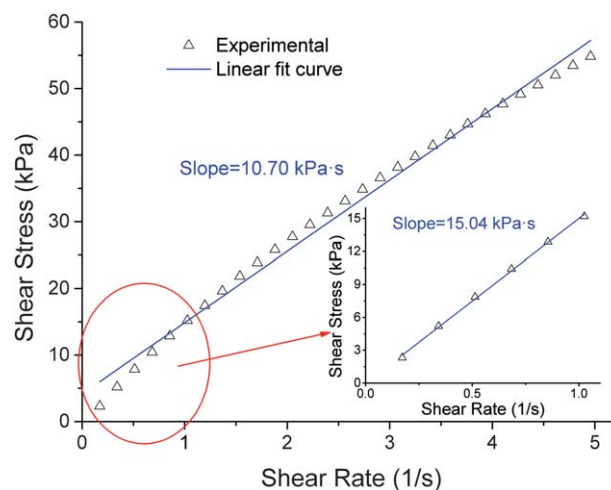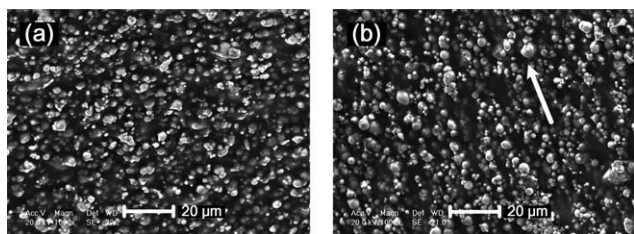

Fig. 3 SEM images of MRP-70: isotropic dispersion (a) and anisotropic chain-like structure (b). The scale bars on the images correspond to 20 microns and the arrow in subfigure (b) denotes the direction of the external magnetic field (Reproduced from Fig. 4 in Xu et al.).[1]

Fig. 4 The viscosity of polyurethane-based MRP with 70 wt% BASF-CIP-CN at 25 °C. The inset shows the shear rate in the range of 0.0–1.0 s^{-1}.

10.70 kPa s, while $\tau_0 = 0.02$ kPa and $\eta = 15.04$ kPa s from the view in the range of 0.0–1.0 s^{-1}. The inset of Fig. 4 indicates that a nonnegligible error exists at a low shear rate when the overall Bingham model is used.

3 Analytical model

In this section, the magnetic moment of a particle in an external uniform magnetic field is determined by its magnetization properties and its volume firstly. Then, the magnetic particle–particle interaction is constructed. At the same time, other particle–particle interactions are also taken into account. The particle–matrix interaction is simplified as that the particle is dragged in the high-viscosity fluid-like matrix with a certain yield stress. Finally, the kinematic equation of a particle will be given according to the forces applied to it.

3.1 The magnetic moment of a particle in a uniform magnetic field

When an iron particle with a diameter d_i is placed into a uniform magnetic field H, the magnetic moment m_i of the particle is:

$$m_i = M \cdot V_i = M_s(1 - e^{-\chi H}) \cdot V_i. \tag{4}$$

Here, the particle is supposed to be magnetized uniformly. M is the magnetization of the iron particle and $V_i = \pi d_i^3/6$ is the volume of particle i. H is the magnetic strength. With a magnetic moment m_i, particle i induces a magnetic field H_i in the surrounding space as:

$$H_i = -\frac{m_i}{4\pi r^3} + \frac{3(m_i \cdot r)r}{4\pi r^5}, \tag{5}$$

where r is the spatial vector from particle i to a spatial field point and r is the norm of r. When another particle j is placed into the

magnetic field H, it will induce a magnetic field H_{ij} on particle i as:

$$H_{ij} = -\frac{m_j}{4\pi r_{ij}^3} + \frac{3(m_j \cdot r_{ij})r_{ij}}{4\pi r_{ij}^5}, \tag{6}$$

where m_j is the magnetic moment of particle j induced by the external magnetic field. r_{ij} is the positional vector from particle j to i and r_{ij} is the norm of r_{ij}. After several magnetization iterations, the magnetized particle system is stable. Then, the magnetic moment of particle i is:

$$m_i = M_s \left[1 - \exp\left(-\chi \left| H + \sum_{j \neq i} H_{ij} \right| \right) \right] V_i, \tag{7}$$

with the direction

$$\hat{m}_i = \hat{M}_s = \frac{H + \sum_{j \neq i} H_{ij}}{\left| H + \sum_{j \neq i} H_{ij} \right|}.$$

Here, linear superposition is supposed. H and H_{ij} are the strength of H and H_{ij}, respectively.

3.2 Particle–particle interaction

The interparticle force of ferromagnetic steel balls in a steady, uniform magnetic field has been measured by Tan and Jones,[32] indicating that linear multipolar expansion can be used to reasonably calculate the interparticle force. In addition, the theoretical analysis of the magnetic interaction between paramagnetic beads has been discussed in detail by Keaveny and Maxey.[33] They introduced an alternative finite-dipole model, where the magnetization of a particle is represented as a distribution of the current density. It is pointed out that higher order multipoles are needed to properly resolve the interaction between two close particles. Though these analytic results are sufficiently accurate, they are difficult to use in large particulate assemblies.

Mainly based on the works above, we propose an easy-to-use modified dipolar force model F_{ij}^m (detailed discussion can be found in the ESI, Section 1†), which is preferred to describe the magnetic interaction force of two close magnetized particles and is presented as:

$$F_{ij}^m = \begin{cases} c_m \cdot F_{ij}^{dipole}, & \text{for } d_{ij} \leq r_{ij} \leq 1.5d_{ij} \\ F_{ij}^{dipole}, & \text{for } r_{ij} > 1.5d_{ij} \end{cases}, \tag{8}$$

$$c_m = 1 + \left(3 - \frac{2r_{ij}}{d_{ij}} \right)^2 \left(\frac{60.17}{1 + e^{(\theta - 34.55)/12.52}} - 22.79 \right) \frac{1}{100}$$

$$F_{ij}^{dipole} = -\frac{3\mu_0}{4\pi r_{ij}^4 \mu_1} \left[(m_i \cdot m_j)\hat{r} - 5(m_i \cdot \hat{r})(m_j \cdot \hat{r})\hat{r} \right. \\ \left. + (m_j \cdot \hat{r})m_i + (m_i \cdot \hat{r})m_j \right]. \tag{9}$$

Here, c_m is the correction factor for adjusting the magnetic dipole model to two close magnetized particles. d_{ij} is the average value of the diameters of two considered particles. θ is the angle between

the direction of the external magnetic field and the relative positional vector. $\hat{r} = r_{ij}/r_{ij}$ and F_{ij}^{dipole} denotes the magnetic interaction force between two magnetic dipoles. μ_0 and μ_1 are the permeability of vacuum and the matrix, respectively. m_i and m_j are the magnetic moment of particles i and j. The other numerical constants are the fitting coefficients from the data analysis. The force error ($c_m - 1$) between the proposed modified model and the conventional dipole model when $r_{ij} = d_{ij}$ is shown in Fig. 5. The error ranges from -23.1% at $\theta = 90°$ to 33.3% at $\theta = 0°$. The interparticle spacing dependent force error is presented in Fig. 6 and the force errors converge to zero when $r_{ij} = d_{ij}$ for all θ.

To avoid the overlap of magnetized particles, the excluded-volume force F_{ij}^{ev} was introduced. This force was calculated by Melle et al. as:[34]

$$F_{ij}^{ev} = A \frac{3\mu_0 m_i \cdot m_j}{4\pi d_{ij}^4} \exp[-\xi(r_{ij}/d_{ij} - 1)] \cdot \hat{r}_{ij}, \tag{10}$$

where $A = 2$ and $\xi = 10$. The parameter A was chosen in order to give zero interaction force when two particles which align along the field direction and interact with the dipolar force are in contact.

The van der Waals force F_{ij}^{vdw} was also taken into account for modelling the particle–particle interaction. This force can be expressed as:[35]

$$F_{ij}^{vdw} = \begin{cases} \dfrac{A}{24} \dfrac{d_{ij}}{(r_{ij} - d_{ij})^2} \hat{r}, & \text{for } r_{ij} - d_{ij} > h_{min} \\[4mm] \dfrac{A}{24} \dfrac{d_{ij}}{h_{min}^2} \hat{r}, & \text{for } r_{ij} - d_{ij} \leq h_{min} \end{cases}, \tag{11}$$

where $A = 5 \times 10^{-19}$ is the Hamaker coefficient, and $h_{min} = 0.001d_{ij}$ was used. Herein, the main particle–particle interaction force model has been established.

3.3 Particle–matrix interaction

As Fig. 4 shows, the shear stress–rate relation of MRP-70 can be described by the Bingham fluid model. When a particle moves in the MRP, it will be hindered by the viscous drag force F_i^d from
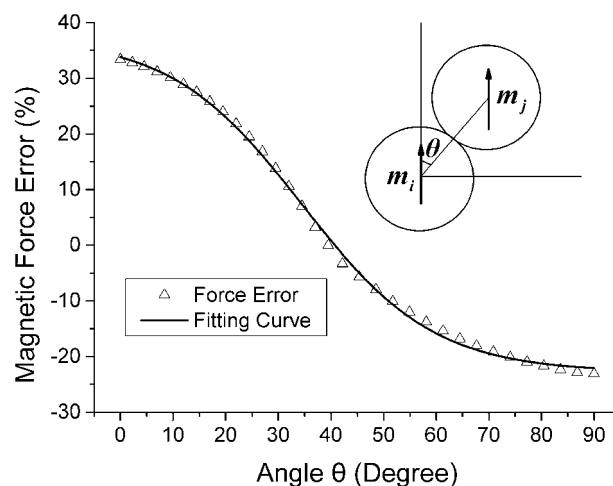
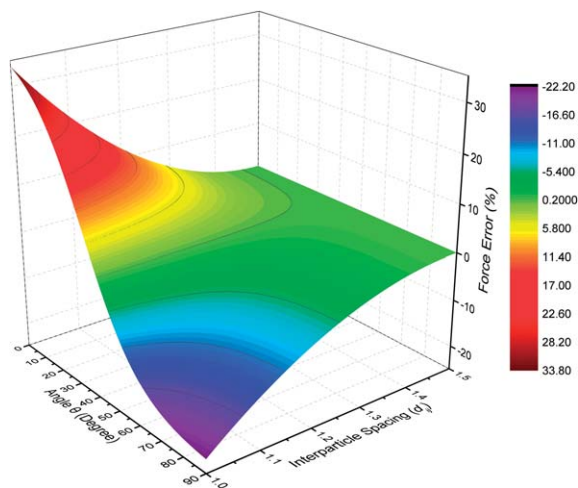**Fig. 5** Magnetic force error when $r_{ij} = d_{ij}$.

Fig. 6 Interparticle spacing and angle dependent force error.

the surrounding MRP. The drag coefficient C_d in the Bingham fluid has been discussed and presented by Li *et al.*[36] The drag coefficient was experimentally tested as $C_d \approx 19/\mathrm{Re}_b$ at a low Reynolds number Re_b with

$$C_d = \frac{F_i^d}{2\pi\rho d_i^2 v^2} \approx \frac{19}{\mathrm{Re}_b} \tag{12}$$

$$\mathrm{Re}_b = \frac{\rho d_i v}{\eta\left(1 + \frac{\tau_0 d_i}{\eta v}\right)}$$

where ρ is the density of the particle and v is the moving velocity of the particle. The drag force can be deduced in vector form as:

$$F_i^d = -\frac{19}{8}\pi\left(\tau_0 d_i^2 \hat{v} + d_i \eta v\right) \tag{13}$$

where $\hat{v}$ is the unit vector along with v.

The force of gravity and buoyancy applied on the particle is:

$$F_i^{gb} = \frac{\pi d_i^2}{6}(\rho - \rho_m)g \tag{14}$$

where ρ_m is the density of the matrix and g is the gravitational acceleration. If the magnitude order of the yield stress is set to $\tau_0 = \mathrm{O}(100)$, then the value of the other variables and can be substituted:

$$\frac{|F_i^{gb}|}{|F_i^d|} = \mathrm{O}(10^{-2}) << 1.0 \quad \text{and} \quad \frac{|F_{ij}^m|}{|F_i^d|} = \mathrm{O}(10^2) >> 1.0 \tag{15}$$

Eqn (15) explains why the particles cannot move in the absence of the external magnetic field and can rearrange into new microstructures with the changing of the external magnetic field.

3.4 Kinematic equation

As BASF-CIP-CN is a soft magnetic material, the magnetic torque applied on the particles is so small that the magneto-induced body rotational motion of the iron particles can be neglected. The inertia effect and stochastic motion of the particles were also not taken into account. This processing is reasonable because the magnetic interaction of the particles dominates their random thermal motion when an external magnetic field is applied rapidly, as was discussed analogously for magnetorheological fluids by Mohebi *et al.*[37] With the aforementioned forces, the kinematic equation can be constructed as:

$$\begin{cases} \dfrac{dr_i}{dt} = \dfrac{1}{\zeta_t}\left[\sum_{j \neq i}(F_{ij}^m + F_{ij}^{ev} + F_{ij}^{vdw}) + F_i^{gb} - \dfrac{19}{8}\pi d_i^2 \tau_0 \hat{v}\right] \\[4pt] \quad \text{for } \left|\sum F_i\right| > \dfrac{19}{8}\pi d_i^2 \tau_0 \\[10pt] \dfrac{dr_i}{dt} = 0, \quad \text{for } \left|\sum F_i\right| \leq \dfrac{19}{8}\pi d_i^2 \tau_0 \end{cases} \tag{16}$$

where $\zeta_t = 19\pi d_i \eta/8$ is the translational drag coefficient and $\sum F_i$ denotes the total forces excluding the viscous drag force from the matrix applied on particle i. eqn (16) can be solved using a numerical method.

To characterize the state of the considered particle assembly, the microstructure dependent magnetic potential energy U^m and the stress tensor σ are presented, respectively. Here, the dipole approximation is still used to give the magnetic potential energy of the whole particle assembly, as the effect of a more accurate magnetic potential model has been involved in the effect of the modified magnetic force model.

$$U^m = \sum_i -\mu_0 m_i \cdot H + \sum_i \sum_{j \neq i} \frac{\mu_0}{4\pi r_{ij}^3}\left[m_i \cdot m_j - 3(m_i \cdot \hat{r})(m_j \cdot \hat{r})\right] \tag{17}$$

$$\sigma = \frac{1}{V}\sum_i \sum_{j \neq i} r_{ij} F_{ij}^m \tag{18}$$

Here, V is the volume of the particulate system under consideration. r_{ij} and F_{ij}^m are the interparticle position vector and the magnetic interaction force, respectively. The magnetic potential energy U^m is constituted of two parts. One is the magnetic potential energy possessed by magnetized particles in the external magnetic field (the first item on the right side of eqn (17)). The other one is the interparticle magnetic potential energy of the magnetized particles (the second item on the right side of eqn (17)). The interparticle magnetic potential energy depends on the distribution of the magnetized particles in the matrix and its variation can directly reflect the evolution of the interior microstructure of the MRP. The stress tensor (as is shown in eqn (18)), which depends on the interparticle positions and forces, can characterize the stress state of the considered particle assembly and can be tested experimentally. The variation of the stress tensor can also reflect the evolution of the interior microstructure of the MRP. In brief, the variation of the magnetic potential energy or the stress state is the reflection of the evolution of the microstructure.

4 Results and discussion

In this section, a cubic cell in the MRP with an edge length of $L = 100$ μm (about $18 \times d_{50}$) is considered. The truncation

radius of the magneto-induced particle–particle interaction is set as $7 \times d_{50}$, which is large enough to count the magneto-induced particle–particle interaction. The configurations of the magneto-induced, rearrangeable microstructure in the MRP in a steady, uniform magnetic field, a stepwise rotating magnetic field, and a spatially changing magnetic field will be presented in sequence. Meanwhile, the microstructure dependent magnetic potential energy or stress tensor will be presented and analysed.

4.1 Magneto-induced microstructure in a steady, uniform, magnetic field

To investigate the evolution of the magneto-induced microstructure of MRP in a vertical, steady, uniform, magnetic field, we take MRP-70 in a magnetic field $H = 391.0$ kA m^{-1} as an example. As Fig. 7 shows, the iron particles in MRP-70 disperse randomly in the initial state (0 s), and then, a steady uniform magnetic field $H = 391.0$ kA m^{-1} is suddenly applied. 5 seconds later, a lot of short chain-like particulate structures are formed quickly. These short chains are made of particles attracting or being attracted to their neighbouring particles. Then, as a result of particles being attracted to other particles or short chains attracting other short chains, long chain-like particulate structures form at 20 s. With the particle–chain and chain–chain interaction proceeding, more stable column-like structures are constructed at 100 s.

It is also significant to know how the microstructure dependent magnetic potential energy and stress state vary with time after applying the external magnetic field to the MRP. To compare this with the results of computational normal stress, a commercial rheometer Physica MCR301 (produced by Anton Paar GmbH, Austria) was used to test the magneto-induced normal stress of MRP. We took the values $H = 193.9$ kA m^{-1}, 391.0 kA m^{-1}, and 740.1 kA m^{-1} in our experiments by

adjusting the current in the electromagnetic device (type MRD180, an accessory of Physica MCR301) as 1.0 A, 2.0 A, and 4.0 A, correspondingly. The maximum magnetic strength of 740.1 kA m^{-1} exceeded the magnetic strength that saturates the magnetization of the carbonyl iron particle. As the magnetization dynamics proceed in milliseconds, we treated the magnetization process of the iron particles as a transient process in the evolution processes. In other words, the particles acquired magnetic moments transiently when applying an external magnetic field, and then the interparticle interactions drove the particles to form certain particulate structures.

Fig. 8 shows the evolution of the magnetic potential energy of MRP-70 over time in different magnetic fields. In this figure, the densities of the energies attain initial transient values of
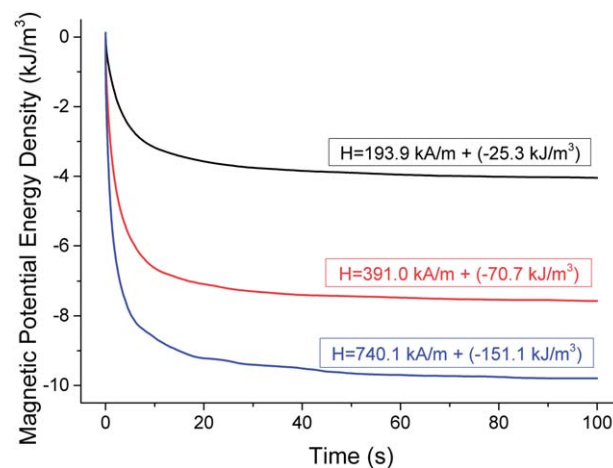

Fig. 8 The evolution of the magnetic potential energy of MRP-70 in different magnetic fields. The values in parentheses of the labels show the initial transient magnetic potential energy densities in a relative magnetic field (*i.e.* the values do not add to relative magnetic fields).
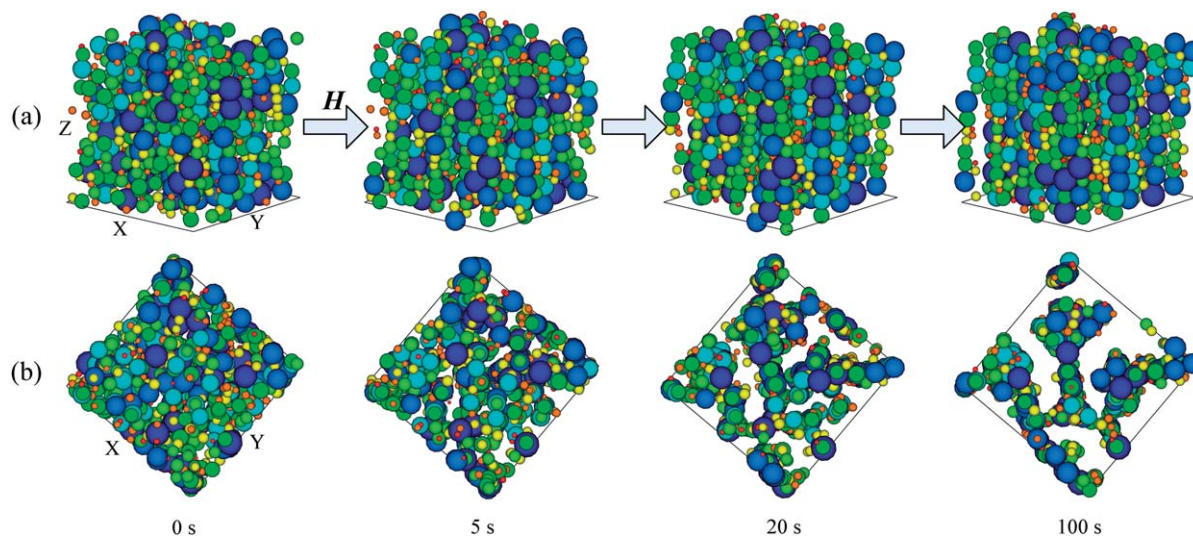

Fig. 7 The evolution of magneto-induced microstructures in MRP-70 in a magnetic field $H = 391.0$ kA m^{-1} with axonometric views (a) and top views (b). The configurations after applying H: randomly dispersing at 0 s, short chains at 5 s, long chains at 20 s, and columns at 100 s. The labels of the considered cellular axes are shown at 0 s and these are the same for the subsequent figures in this paper unless otherwise specified.

-25.3 kJ m^{-3}, -70.7 kJ m^{-3} and -151.1 kJ m^{-3} (as shown in the parentheses of the labels) when applying the magnetic field $H = 193.9$ kA m^{-1}, 391.0 kA m^{-1}, and 740.1 kA m^{-1}, respectively. Then, they drop down sharply in the incipient 10 seconds. In the meantime, the very complex magneto-mechanical coupling process proceeds. With proceeding time, the magnetic potential energies decrease to the respective stable values, and more stable magneto-induced microstructures are achieved gradually. The stronger the external magnetic field, the lower the magnetic potential energy and the deeper the energy drops. Fig. 9 shows the evolution of the vertical normal stress of MRP-70 in different magnetic fields $H = 193.9$ kA m^{-1}, 391.0 kA m^{-1}, and 740.1 kA m^{-1}. It can be seen that the microstructure dependent computational normal stresses are in good agreement with the relative experimental results as a whole, indicating the simulations are rational. The normal stress can reach as high as 60.2 kPa in a magnetic field of 740.1 kA m^{-1}. This shows the high potential of magneto-controllable performance of MRP.

In addition, the microstructures of the MRP in a steady, uniform magnetic field $H = 740.1$ kA m^{-1} with different volume fractions are shown in Fig. 10. Here, we use $H = 740.1$ kA m^{-1} to magnetize the iron particles sufficiently. When the volume fraction is small, such as $\varphi = 5.0\%$, short and long chains both exist in the considered cubic cell and they separate from each other, though there is a small number of particles that disperse singly. When the volume fraction increases to about 15.0%, long chains are the main particulate structures and almost no single particles exist in the cubic cell. In addition, they also exist in the MRP with a volume fraction of 15%. As for the MRP with a volume fraction of 24.2%, column-like structures are the main existing form. More stable column-like structures are constructed for the MRP with a volume fraction of 35.0% because the particle–chain and chain–chain interactions get stronger with increasing particle number in the cubic cell. Relating to Fig. 10, the evolution of the magnetic potential energy and normal stress with different volume fractions in a magnetic field $H = 740.1$ kA m^{-1} are shown in Fig. 11. It can be seen

Fig. 10 The volume fraction φ dependent stable microstructures in a magnetic field of $H = 740.1$ kA m^{-1}.

directly that the larger the volume fraction is, the lower the magnetic potential energy and the stronger the normal stress will be. The magnetic potential energies attain transient initial values of -31.3 kJ m^{-3}, -93.9 kJ m^{-3}, -151.1 kJ m^{-3}, and -219.7 kJ m^{-3}, relating to the volume fraction φ of 5.0%, 15.0%, 24.2%, and 35.0%, respectively. Then the energies drop slightly and stabilize quickly. The saturated vertical normal stress of MRP with different volume fractions of 5.0%, 15.0%, 24.2%, and 35.0% can reach 16.5 kPa, 40.4 kPa, 60.2 kPa, and 70.5 kPa, respectively. The stresses change fast in the incipient 20 seconds and approach each certain stable value gradually.

4.2 Magneto-induced microstructures in a stepwise in-plane rotating magnetic field

In the previous subsection, it was noticed that magneto-induced microstructures change dramatically in the incipient 10 seconds and stabilize within about 50 seconds of applying the external magnetic field. It is interesting to study how the
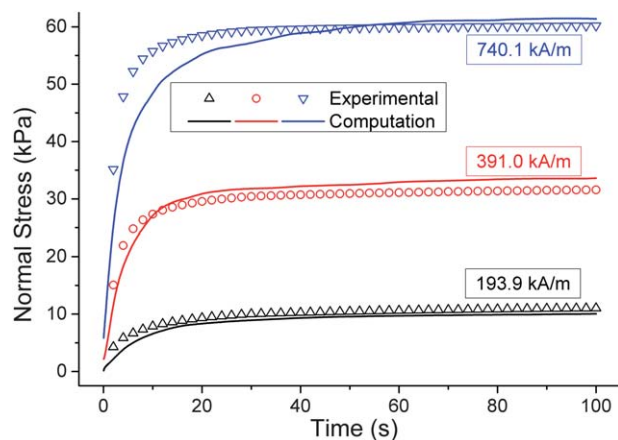

Fig. 9 The evolution of normal stress of MRP-70 in different magnetic fields. The solid lines resemble the computational results while the open symbols resemble the results of experimental tests.
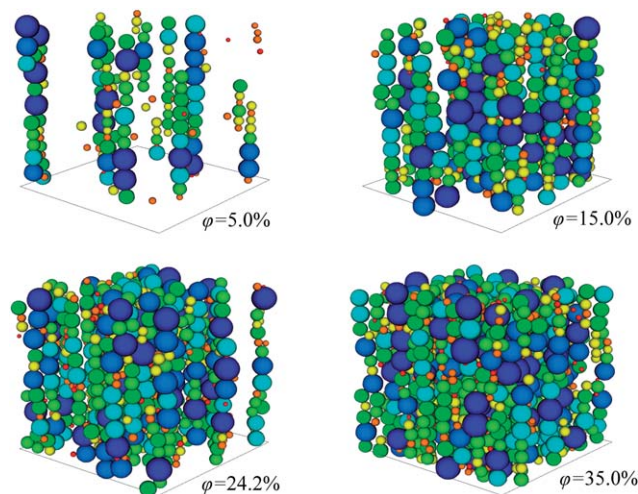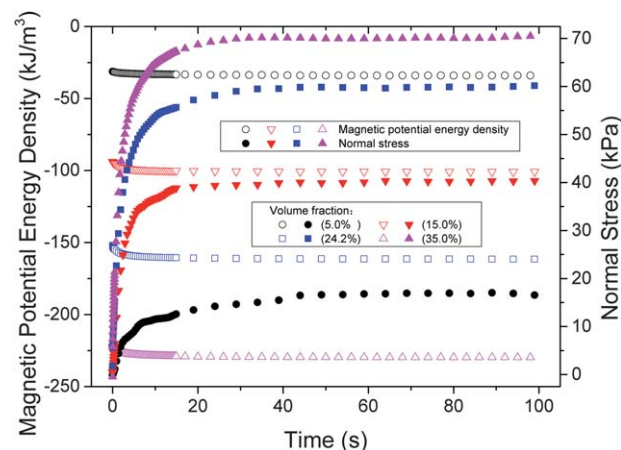

Fig. 11 The evolution of the magnetic potential energy and normal stress in the magnetic field of $H = 740.1$ kA m^{-1} with different volume fractions φ.

magneto-induced microstructures will perform if we change the external magnetic field every 10 seconds. To do this, we set a stepwise changing magnetic field as:

$$\begin{cases} \boldsymbol{H}_x = \sin(2\pi t_n/120)H \cdot \hat{\boldsymbol{x}} \\ \boldsymbol{H}_y = 0\hat{\boldsymbol{y}} \\ \boldsymbol{H}_z = \cos(2\pi t_n/120)H \cdot \hat{\boldsymbol{z}} \end{cases}. \quad (19)$$

The external magnetic field $\boldsymbol{H}$ changes its orientation in the ZX plane with a constant strength H. $t_n = t_{n-1} + \Delta t (n = 1,2,3,\cdots,12)$ with an initial $t_0 = 0$ s and an interval $\Delta t = 10$ s. $\hat{\boldsymbol{x}}, \hat{\boldsymbol{y}}$ and $\hat{\boldsymbol{z}}$ are the unit vectors along the X, Y, and Z axes in Fig. 7, respectively.

Fig. 12 shows the magneto-induced microstructures along with a stepwise rotating magnetic field with the strength $H = 391.0$ kA m^{-1}. In the first 10 seconds, short chains appear along the vertical external magnetic field quickly. Then, the orientation of the magnetic field was rotated clockwise by 30 degrees in the ZX plane and kept for the next 10 seconds. The subsequent rotations were performed in the same way. The short chains gradually inclined towards the rotated magnetic field step by step and got longer and longer. At the 40th second, the short particulate chains turned into long chains and orientated along the X axis as the magnetic field rotated along the X axis. Then, an interesting phenomenon occurred. The particles aggregated into two separated assemblies in the next twenty seconds, and layered structures parallel to the rotating plane of the magnetic field were constructed gradually with time.

To our knowledge, flow-induced layered patterns have been presented experimentally and the effects of the magnetic dipolar interactions in the alternating magnetic fields have been discussed.[38–40] This study is the first one to give the direct simulation results of magneto-induced layered structures in a stepwise rotating magnetic field. This phenomenon can be understood as the attraction of two magnetized particles with different configurations when $|\cos(\theta)| > \sqrt{5}/5$ (θ is the angle between the direction of the external magnetic field and the direction of the relative position vector of the two particles), as well as the repulsiveness of two magnetized particles with the configurations when $|\cos(\theta)| < \sqrt{5}/5$ (a detailed discussion can be found in ESI, Section 2†).

It can be noticed from Fig. 12 that the particulate microstructure in MRP can be controlled by changing the external magnetic field. However, it is inconvenient to unambiguously estimate the mechanism of those complex processes if the external magnetic field changes too fast. Then, we focused on the magneto-induced rearrangeable microstructure from one steady state to another. We changed the external magnetic field step by step and kept it constant for enough time in one step to get a stable particulate structure. To do this, a new stepwise changing magnetic field with long-time intervals was set as:

$$\begin{cases} \boldsymbol{H}_x = \sin(2\pi t_n/800)H \cdot \hat{\boldsymbol{x}} \\ \boldsymbol{H}_y = 0\hat{\boldsymbol{y}} \\ \boldsymbol{H}_z = \cos(2\pi t_n/800)H \cdot \hat{\boldsymbol{z}} \end{cases}. \quad (20)$$

in which $t_n = t_{n-1} + \Delta t (n = 1,2,3,\cdots,8)$ with an initial $t_0 = 0$ and an interval $\Delta t = 100$ seconds. Fig. 13 shows that the magneto-induced microstructure evolves with an external magnetic field from one steady state to another. In the first 100 second interval, iron particles form stable column-like vertical structures. Then, when the magnetic field is rotated clockwise by 45 degrees in the ZX plane, the columns incline towards the magnetic field gradually. The final structure of this step is shown as the second subfigure in Fig. 13(a). Continuing the rotation of the magnetic field by another 45 degrees in the ZX plane, the magnetic field orientates towards the X-axis. 100 seconds later, it is found that the particles separate into two parts and form two thick layered structures in the rotating plane (ZX plane) of the magnetic field, though these two thick layered structures are loose-knit. By continuing to rotate the magnetic field step by step, the layered structures get more and more well-knit. Several particles at the right and upper-right of the top view at 900 s are actually attached to the bottom-left particle layer as a result of the periodic boundary condition.

With the evolution of microstructures, the magnetic potential energies evolve with time in different magnetic fields as shown in Fig. 14. Analogous to Fig. 8, the magnetic potential energy densities attain initial values of -25.3 kJ m^{-3}, -68.7 kJ m^{-3}, and -145.1 kJ m^{-3} (as shown in the parentheses of the labels) in different magnetic fields of 193.9 kA m^{-1}, 391.0 kA m^{-1}, and 740.1 kA m^{-1}, respectively. The stronger the external magnetic field is, the lower the magnetic potential energy will be. In the first 100 second interval, the magnetic potential energy drops abruptly from the initial state and gradually approaches a stable state. Meanwhile, the particulate
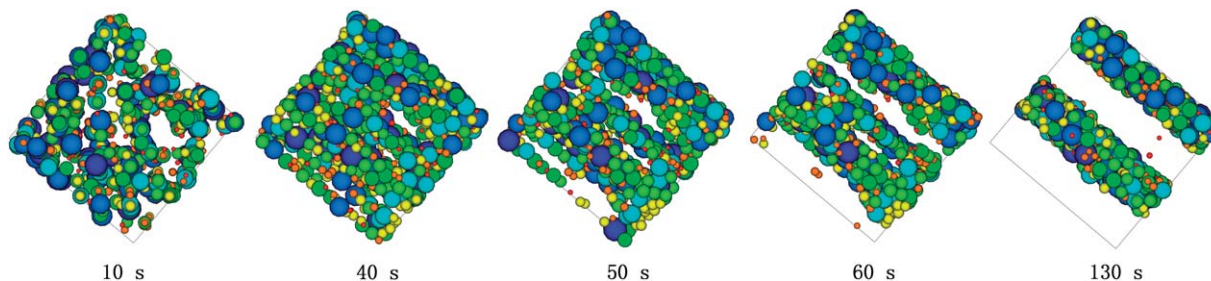

| 10 s | 40 s | 50 s | 60 s | 130 s |

Fig. 12 The top views of the magneto-induced microstructure of MRP-70 *versus* time in a stepwise in-plane rotating magnetic field with strength $H = 391.0$ kA m^{-1} and an interval of $\Delta t = 10$ seconds.

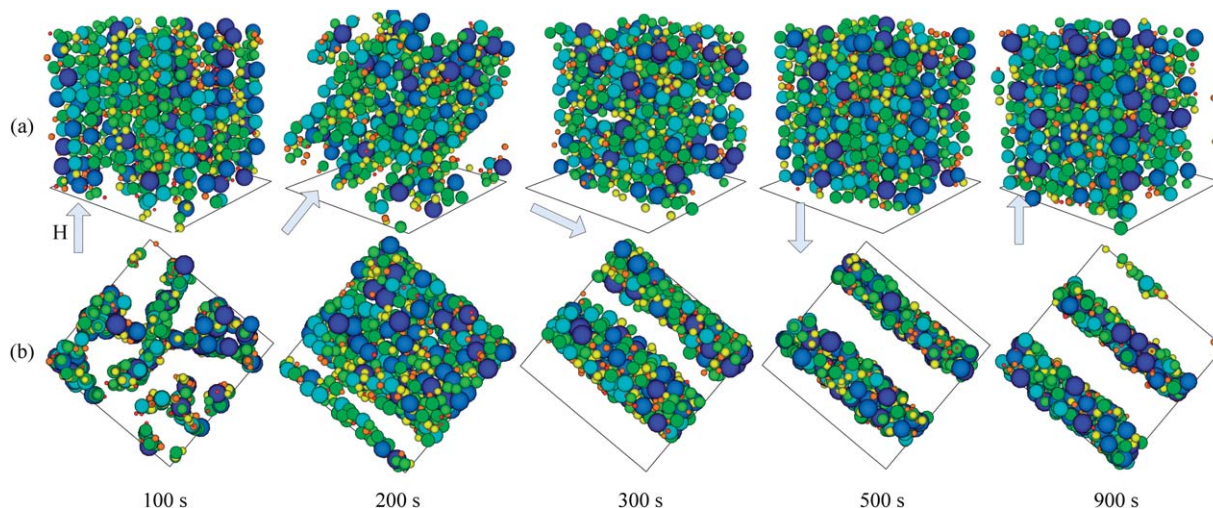**Fig. 13** The magneto-induced microstructure *versus* time of MRP-70 in a stepwise in-plane rotating magnetic field with the strength $H = 391.0$ kA m^{-1} and an interval $\Delta t = 100$ seconds. The figures show the axonometric views (a) and top views (b). The arrows denote the direction of the external magnetic field.
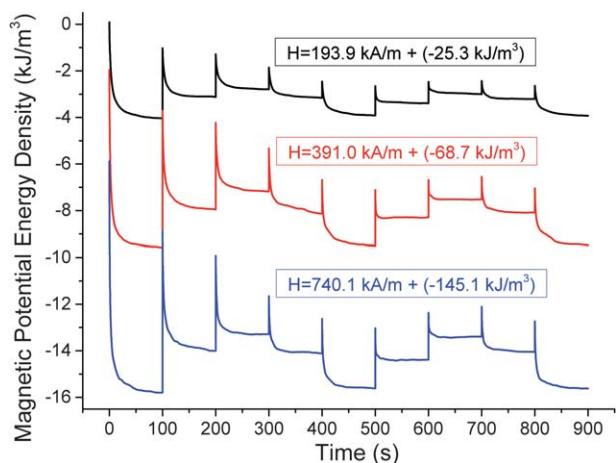

Fig. 14 The magnetic potential energy *versus* time of MRP-70 in a stepwise rotating magnetic field with a turning interval $\Delta t = 100$ seconds.

microstructure gets more and more stable. When the external magnetic field is transiently rotated by 45° in the *ZX* plane at the 100th second, the iron particle assembly acquires a transient power and shows much motion. But the assembly cools down gradually in the short-lived steady external magnetic field. For every rotating step, the magnetic potential energy adheres to the principle of minimum potential energy. These processes are the same for the subsequent transient rotations of the external magnetic field. Moreover, the magnetic potential energy shows a periodic change with the rotating of the external magnetic field. This phenomenon relates to the configuration between the particle assembly in the considered cubic cell and the external magnetic field.

The magneto-induced microstructures of the MRP with different volume fractions at $H = 740.1$ kA m^{-1} are shown in Fig. 15. Parallel layered structures are formed for all the volume fractions of 5.0%, 15.0%, 24.2%, and 35.0%. Monolayer structures appear in the MRP with small volume fractions (*e.g.* $\varphi =$

5.0%), though the particles in the same plane are evenly separated. When the volume fraction increases to about 15.0%, an unseparated layered structure is constructed. With the volume fraction increasing, the particulate layer gets thicker and the layer–layer gap gets smaller. In addition, the particulate layered structure also gets more well-knit with increasing volume fraction. Corresponding to the evolution of the microstructure, the evolution of the microstructure dependent magnetic potential energy of MRP with different volume fractions at $H = 740.1$ kA m^{-1} is shown as Fig. 16. It can be seen directly that the larger the volume fraction is, the lower the magnetic potential energy will be. The evolution process of the magnetic potential energy for a certain volume fraction is similar to the one described in Fig. 14.
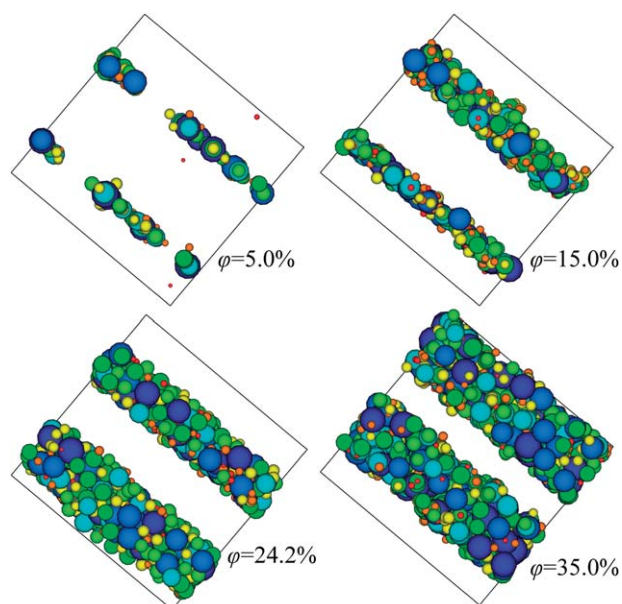

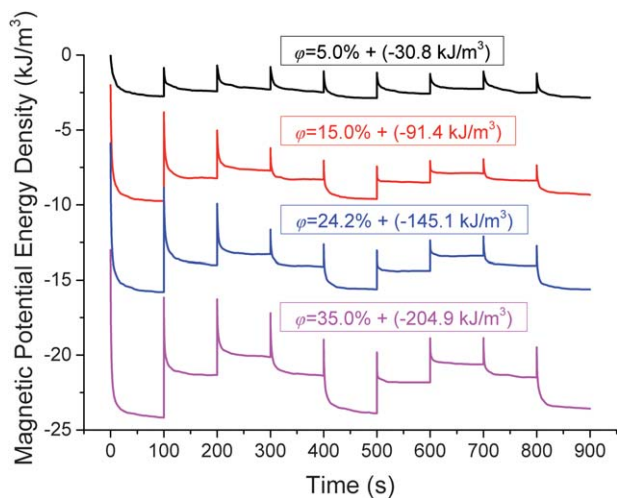**Fig. 15** Magneto-induced microstructures of MRP with different volume fractions at $H = 740.1$ kA m^{-1}.

Fig. 16 Volume fraction φ dependent magnetic potential energy at $H = 740.1$ kA m^{-1}.

4.3 Magneto-induced microstructures in a spatially changing magnetic field

To investigate the evolution of the magneto-induced particulate microstructures of MRP in a spatially changing magnetic field, several different changing processes were simulated and two typical processes are shown in Fig. 17. There are five steps in one change series and the labels (x), (y), and (z) under the subfigures denote the direction of the external magnetic field orientating towards the X, Y, and Z axis, respectively. The XY plane is indicated by a quadrilateral and the Z axis is perpendicular to the XY plane. The upper series (Fig. 17(a)) shows the microstructure of MRP-70 changing with the external magnetic field from the initial (z) direction to the final (z) direction. We denote this process as "ZXYXZ". Analogously, the lower series

(Fig. 17(b)) is denoted as "ZYXYX". In Fig. 17, the viewpoint of each subfigure is selected to best observe the particulate structure.

In the process of "ZXYXZ", vertical column-like structures are formed at the end of the first 100 second step. Then, the direction of external magnetic field is transiently changed towards the X axis. 100 seconds later, the particles formt two thick but not very well-knit layered structures in the rotation plane of the magnetic field (ZX plane). By changing the magnetic field towards the Y axis for a next 100 seconds, column-like particulate structures are obtained again, but orientate towards the Y axis. Finally, by orientating the magnetic field returning to the Z axis, vertical layered structures in the ZX plane appear again though they are not so well-knit. In the process of "ZYXYX", the particulate structure changes from the initial vertical disordered column-like structure to the final two horizontal parallel separated well-knit layered structure. The two processes mainly differ in the final step, but have very different final particulate structures.

The magneto-induced microstructure dependent magnetic potential energy of the above two processes is shown in Fig. 18. For the process "ZXYXZ", the magnetic potential energy acquires a transient power at the initial point or the transient turning point of the external magnetic field. Then the magnetic potential energy abruptly drops and gradually approaches a certain stable value. The curve of the magnetic potential energy can reflect the evolution process of the magneto-induced microstructure. The larger the transient variation at the turning point of the external magnetic field and the larger the distinction of the approached stable value, the more different the stable magneto-induced microstructure. As the processes of "ZXYXZ" and "ZYXYX" are mainly different in the final step, the magnetic potential energy curves show high differences in the final step.
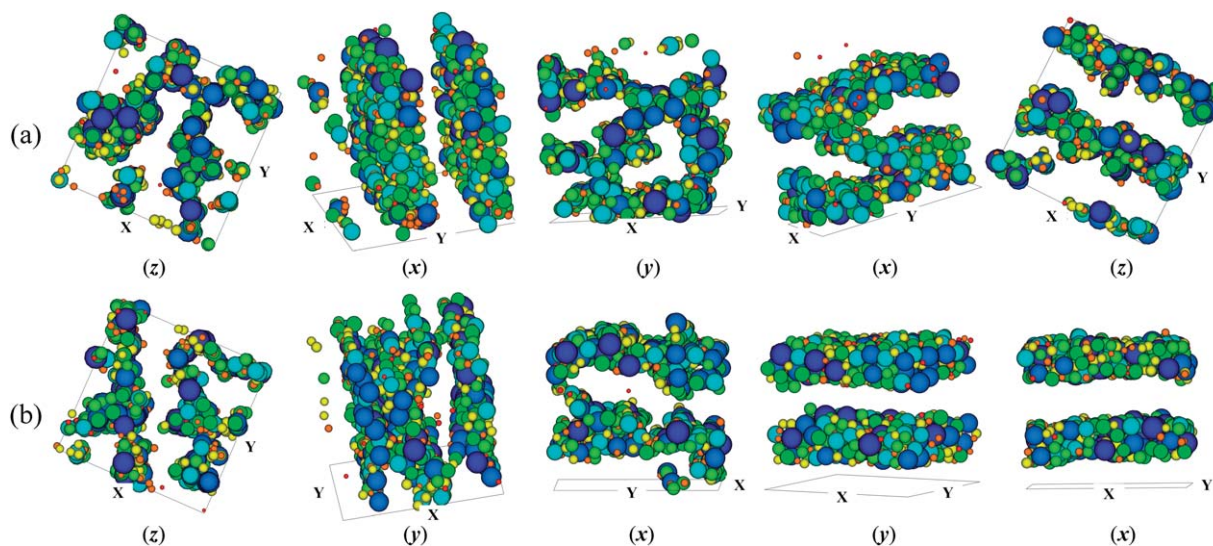

Fig. 17 The evolution of magneto-induced microstructures in MRP-70 in a spatially changing magnetic field with the magnetic strength $H = 740.1$ kA m^{-1}. There are five steps in one series of changes (upper series (a) or lower series (b)) with intervals of 100 seconds. The labels (x), (y), and (z) under the subfigures denote the direction of the external magnetic field orientating towards the X, Y, and Z axis, respectively.
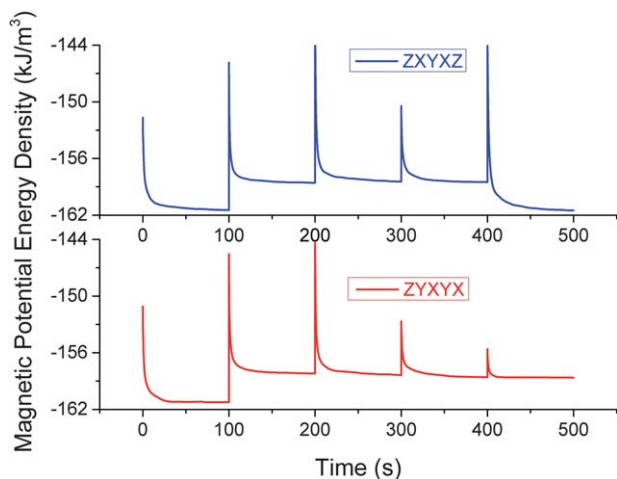
Fig. 18 The magnetic potential energies of MRP-70 evolving over time.

Being dependent on the evolution of the microstructure, Fig. 19 shows the evolution of the mean axial stress over time. The mean axial stress is defined as:

$$[\sigma] = \frac{1}{3}\left(\sigma_{xx} + \sigma_{yy} + \sigma_{zz}\right), \tag{21}$$

where σ_{xx}, σ_{yy}, and σ_{zz} are the axial normal stress components of the stress tensor σ along the X, Y, and Z axis, respectively. In mechanics, $I_1 = \sigma_{xx} + \sigma_{yy} + \sigma_{zz}$ is the first invariant of the stress tensor, which can characterize the volumetric stress strength by considering the cubic cell as a whole. We can qualitatively recognize that the larger the variation of mean axial stress $[\sigma]$ is, the more different the magneto-induced microstructures are.

The first 100 second stage in Fig. 19 relates to MRP-70 in a magnetic field in Z direction. The mean axial stress is almost equal to the normal stress σ_{zz}. The stresses are strengthened sharply at the beginning, reflecting the interior microstructures have dramatic changes (from an initial random dispersing state to a subsequent chain-like dispersing state). With time going by, the stresses attain stable values, reflecting that the interior microstructures stabilize gradually. When the external
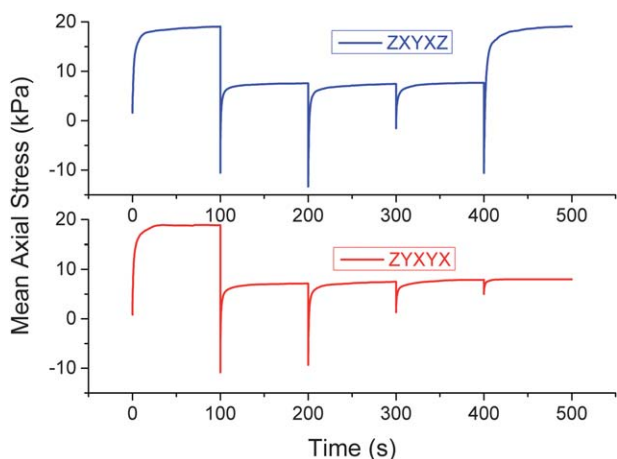
magnetic field is suddenly rotated, the stresses drop abruptly, as the previous tensing chain-like or column-like structures not only loosen suddenly, but also contract oppositely. The stress becomes largely varied if the magnetic field is suddenly changed to being perpendicular to the previous rotating plane of the magnetic field. This process is synchronous with the changing of the microstructure and the magnetic potential energy. Comparing Fig. 18 and 19, it can be seen that the magnetic potential energy and stress tensor are associated, as they are both a reflection of the evolution of the microstructure.

5 Conclusions

In this work, we used a particle-level dynamics simulation to study the magneto-induced microstructure in magneto-rheological plastomers, and put special emphasis on the magneto-induced rearrangeable particulate structure in an external changing magnetic field. When MRP are placed into a steady uniform magnetic field, the soft magnetic particles in the MRP form short chain-like structures quickly, followed by long chain-like and final column-like structures along the direction of the external magnetic field. When MRP are subjected to a stepwise in-plane rotating magnetic field with a constant strength, the magneto-induced interior microstructure rearranges to form a layered structure parallel to the rotating plane of the magnetic field. In the meantime, the microstructure dependent magnetic potential energy and stress state vary sharply at the beginning and then gradually approach respective stable values in every changing step of the external magnetic field. When the external magnetic field is spatially changed step by step, the soft magnetic particles in MRP can rearrange to form column-like structures with different orientations, layered structures with different thickness and orientations and other complex structures. These phenomena can motivate us to produce magneto-controllable microstructures of MRP for potential practical applications.

Fig. 19 The mean axial stresses of MRP-70 evolving over time.

Notes and references

1 Y. G. Xu, X. L. Gong, S. H. Xuan, W. Zhang and Y. C. Fan, *Soft Matter*, 2011, **7**, 5246.
2 Y. G. Xu, X. L. Gong, S. H. Xuan, X. F. Li, L. J. Qin and W. Q. Jiang, *Soft Matter*, 2012, **8**, 8483.
3 X. L. Gong, Y. G. Xu, S. H. Xuan, C. Y. Guo, L. H. Zong and W. Q. Jiang, *J. Rheol.*, 2012, **56**, 1375.
4 C. L. A. Berli and J. de Vicente, *Appl. Phys. Lett.*, 2012, **101**, 021903.
5 B. J. Park, F. F. Fang and H. J. Choi, *Soft Matter*, 2010, **6**, 5246.

6 J. de Vicente, D. J. Klingenberg and R. Hidalgo-Alvarez, *Soft Matter*, 2011, **7**, 3701.

7 G. Bossis, S. Lacis, A. Meunier and O. Volkova, *J. Magn. Magn. Mater.*, 2002, **252**, 224.

8 Y. B. Peng, R. Ghanem and J. Li, *J. Intell. Mater. Syst. Struct.*, 2012, **23**, 1351–1370.

9 Y. Shen, M. F. Golnaraghi and G. R. Heppler, *J. Intell. Mater. Syst. Struct.*, 2004, **15**, 27.

10 W. H. Li and X. Z. Zhang, *Smart Mater. Struct.*, 2010, **19**, 035002.

11 T. F. Tian, W. H. Li, G. Alici, H. Du and Y. M. Deng, *Rheol. Acta*, 2011, **50**, 825.

12 L. Chen and S. Jerrams, *J. Appl. Phys.*, 2011, **110**, 013513.

13 H. N. An, S. J. Picken and E. Mendes, *Soft Matter*, 2012, **8**, 11995.

14 H. N. An, B. Sun, S. J. Picken and E. Mendes, *J. Phys. Chem. B*, 2012, **116**, 4702.

15 P. V. Rao, S. Maniprakash, S. M. Srinivasan and A. R. Srinivasa, *Smart Mater. Struct.*, 2010, **19**, 085019.

16 B. Wei, X. L. Gong, W. Q. Jiang, L. J. Qin and Y. C. Fan, *J. Appl. Polym. Sci.*, 2010, **118**, 2765.

17 S. H. Xuan, Y. L. Zhang, Y. F. Zhou, W. Q. Jiang and X. L. Gong, *J. Mater. Chem.*, 2012, **22**, 13395.

18 J. D. Carlson and M. R. Jolly, *Mechatronics*, 2000, **10**, 555.

19 Q. C. Gong, J. K. Wu, X. L. Gong, Y. C. Fan and H. S. Xia, *RSC Adv.*, 2013, **3**, 3241.

20 J. J. Zhang, L. Li, G. Chen and P. Wee, *Polym. Degrad. Stab.*, 2009, **94**, 246.

21 I. Bica, Y. D. Liu and H. J. Choi, *J. Ind. Eng. Chem.*, 2013, **19**, 394.

22 Y. C. Li, J. C. Li, W. H. Li and B. Samali, *Smart Mater. Struct.*, 2013, **22**, 035005.

23 G. Bossis, L. Iskakova, V. Kostenko and A. Zubarev, *Phys. A*, 2011, **390**, 2655.

24 A. Y. Zubarev and L. Y. Iskakova, *Phys. A*, 2007, **382**, 378.

25 A. Gomez-Ramirez, M. T. Lopez-Lopez, J. D. G. Duran and F. Gonzalez-Caballero, *Soft Matter*, 2009, **5**, 3888.

26 G. Bossis, P. Lancon, A. Meunier, L. Iskakova, V. Kostenko and A. Zubarev, *Phys. A*, 2013, **392**, 1567.

27 T. X. Liu, R. Gu, X. L. Gong, S. H. Xuan, H. G. Wu and Z. Zhang, *Magnetohydrodynamics*, 2010, **46**, 257.

28 Y. Enomoto, K. Oba and M. Okada, *Phys. A*, 2003, **330**, 496.

29 V. Q. Nguyen, A. S. Ahmed and R. V. Ramanujan, *Adv. Mater.*, 2012, **24**, 4041.

30 I. B. Jang, H. B. Kim, J. Y. Lee, J. L. You, H. J. Choi and M. S. Jhon, *J. Appl. Phys.*, 2005, **97**, 10Q912.

31 L. Chen, X. L. Gong and W. H. Li, *Smart Mater. Struct.*, 2007, **16**, 2645.

32 C. Tan and T. B. Jones, *J. Appl. Phys.*, 1993, **73**, 3593.

33 E. E. Keaveny and M. R. Maxey, *J. Comput. Phys.*, 2008, **227**, 9554.

34 S. Melle, O. G. Calderón, M. A. Rubio and G. G. Fuller, *J. Non-Newtonian Fluid Mech.*, 2002, **102**, 135.

35 D. J. Klingenberg, C. H. Olk, M. A. Golden and J. C. Ulicny, *J. Phys.: Condens. Matter*, 2010, **22**, 324101.

36 C. H. Li, Y. L. Zhang, W. L. Song and W. L. Kang, *J. Daqing Pet. Inst.*, 1995, **19**, 6.

37 M. Mohebi, N. Jamasbi and J. Liu, *Phys. Rev. E: Stat. Phys., Plasmas, Fluids, Relat. Interdiscip. Top.*, 1996, **54**, 5407.

38 O. Volkova, S. Cutillas, P. Carletto, G. Bossis, A. Cebers and A. Meunier, *J. Magn. Magn. Mater.*, 1999, **201**, 66.

39 S. Cutillas, G. Bossis and A. Cebers, *Phys. Rev. E: Stat. Phys., Plasmas, Fluids, Relat. Interdiscip. Top.*, 1998, **57**, 804.

40 G. Bossis and A. Cebers, *J. Magn. Magn. Mater.*, 1999, **201**, 218.